Journal of Applied Fluid Mechanics, Vol. 16, No. 8, pp. 1587-1600, 2023.
Available online at www.jafmonline.net, ISSN 1735-3572, EISSN 1735-3645.
https://doi.org/10.47176/jafm.16.08.1725

Explorative Gradient Method-Based Research on the Optimization of Nozzle Flow-guiding Devices

Y. Wang, L. Huang, Q. Jia† and Z. Yang

School of Automotive Studies, Tongji University, 4800 Cao An Rd., Jiading, Shanghai 201804, China
Shanghai Key Lab of Vehicle Aerodynamics and Vehicle Thermal Management Systems, Tongji University, 4800 Cao An Rd., Jiading, Shanghai 201804, China

† *Corresponding Author Email: qing.jia@sawtc.com*

ABSTRACT

Low-frequency buffeting is a common problem in automobile wind tunnels, it induces pulsations of pressure and velocity in the test section. A 1:15 3/4 open-jet return-type scaled wind tunnel was used for this research, and numerical simulations and tests were implemented to study the flow characteristics of the jet shear layer in a model wind tunnel. The results show that guide devices on the inner wall of the nozzle can effectively reduce the low-frequency buffeting, but the presence of the devices deteriorated the axial static pressure gradient of the flow in the test section. The shape of the guide devices was optimized through the Explorative Gradient Method, and numerical simulations were carried out. An optimal shape can effectively reduce the low-frequency buffeting and ensure flow field uniformity in the test section. Finally, the reliability of the numerical simulation and the practicability of the optimal case were verified through a hot wire test and a microphone test.

Article History

Received December 18, 2022
Revised February 15, 2023
Accepted April 3, 2023
Available online May 31, 2023

Keywords:

Optimization
Low-frequency fluctuations
Spectrum analysis
Jet shear layer
Vortex
Wind tunnel

1. INTRODUCTION

Nowadays, energy issues are becoming more and more prominent. The question of how to reduce the energy consumed by cars is important. The development of the modern automobile industry is changing rapidly with the fast advancement of science and technology, and one important test-based method for improving the performance of a vehicle is the aerodynamic–acoustic wind tunnel test. The effectiveness and accuracy of the wind tunnel test are related to the low-frequency buffeting phenomenon. The accuracy of acoustic and aerodynamic measurements in wind tunnels is important to the designing of vehicles with low drag. In the design of low-drag and -noise vehicles, accurate measurement of the drag coefficient and the noise generated by the vehicle helps to more accurately improve the design, which can reduce the wind noise and drag generated by the vehicle, thus reducing energy consumption.

The main structures of the test section of the wind tunnel are the nozzle, the plenum, and the collector. The jet flow from the nozzle will cause the vortex to fall off. If the flow mode of the jet shear layer, which is formed via the interaction with the collector, matches the natural acoustic mode of the wind tunnel's structure, resonance will occur, causing a strong periodic pulsation in the entire flow field (Künstner et al., 1995). Due to the presence of a plenum in a 3/4 open-jet wind tunnel, a unique low-frequency buffeting phenomenon occurs (Amandolèse & Vartanian 2010). The measurement accuracy in a wind tunnel test will be affected by the low-frequency buffeting phenomenon. Additionally, severe low-frequency buffeting will generate dangerous additional loads and cause permanent damage to the wind tunnel structure.

The current methods for controlling the low-frequency buffeting phenomenon are divided into two types: passive control and active control. Passive control means improving the structure of the wind tunnel to suppress low-frequency buffeting, e.g., implementing vortex generators at the nozzle, changing the angle of the collector and the length of the test section, etc. The DNW-NWB wind tunnel uses Seiferth wings, a type of vortex generator, to reduce the high-amplitude pressure fluctuation caused by the low-frequency buffeting phenomenon (Pott-Pollenske et al., 2012). In 2010, the S2A wind tunnel was tested with a rectangular spoiler at the nozzle to reduce the intensity of pressure fluctuation (Amandolèse & Vartanian 2010). In 2014, Stoll and his colleagues implemented an FKFS-besst on the inner wall of the nozzle in a full-scale aero-acoustic wind tunnel at the University of Stuttgart, which effectively reduced the low-frequency buffeting phenomenon (Stoll & Wiedemann 2018), and a detailed study of the besst was

Nomenclature

Cp	pressure gradient	*PSD*	Power Spectrum Density
Dh	equivalent hydraulic diameter	*RANS*	Reynolds-Averaged Navier–Stokes
EGM	Explorative Gradient Method	*Re*	Reynolds number
FFT	Fast Fourier Transform	*SAWTC*	Shanghai Automotive Wind Tunnel Center
LHS	Latin Hypercube Sampling	*U*	X component of the velocity
OASPL	Overall Sound Pressure Level	*W*	Z component of the velocity
POD	Proper Orthogonal Decomposition	*WALE*	Wall-Adapting Local Eddy-viscosity

conducted in the following work (Blumrich et al., 2015). In order to not affect the acoustic performance and the uniformity of the flow field in the wind tunnel, while also significantly suppressing the periodic pressure fluctuation, an active control method has been proposed. The Audi Acoustics wind tunnel used the ARC system to effectively control the resonance in wind tunnel ducts (Evert & Miehling 2004). Jia et al. (2021) used an acoustically excited synthetic jet exciter to actively control the nozzle jet. By interfering with the vortex separation of the shear layer at the nozzle, they effectively suppressed the low-frequency buffeting of the scaled wind tunnel and improved the flow field quality in the test section.

When studying the shapes of passive vortex generators, various gradient-based optimization algorithms are usually used. In gradient algorithm-based optimization research, the Downhill Simplex Method, the most robust representative algorithm, is a simple, robust, and widely used method (Nelder & Mead 1965). It uses the gradient information of the surrounding points to descend to the local optimum, with high efficiency and good convergence, but the algorithm easily falls into the local optimum (Press et al., 2007). On the other hand, Latin Hypercube Sampling (LHS) explores the entire domain independently of the cost value, which is more able to approach the global minimum (McKay et al., 2000). Therefore, Li et al. (2022) designed a new intelligent algorithm to achieve the purpose of efficient optimization, namely, the Explorative Gradient Method (EGM). Learning from the idea of the genetic algorithm, the EGM algorithm deals with high-dimensional parameter space, uses the Downhill Simplex Method to explore local areas, and at the same time conducts uniform explorations throughout the entire parameter space through LHS.

Based on the structural characteristics of the 3/4 open-jet aero-acoustic wind tunnel at the Shanghai Automotive Wind Tunnel Center (SAWTC), this paper designed a type of guide device inside the nozzle and took a 1:15 scaled wind tunnel as the research object. We planned to use numerical and experimental methods to study the wind tunnel buffeting phenomenon. First of all, the influence of the guide devices on the flow field in the wind tunnel plenum was explored. Furthermore, its inhibiting effect on low-frequency buffeting was analyzed. Then the EGM algorithm was used to optimize the shape of the guide devices, and we finally achieved the target of suppressing the low-frequency buffeting phenomenon while ensuring good flow field uniformity.

2. METHODOLOGY

2.1 Numerical Setup

To reduce the occurrence of low-frequency buffeting and pressure pulsation in the wind tunnel, a type of passive vortex generator was designed and optimized. Its effect on the flow structure in the jet shear layer and the low-frequency buffeting phenomenon was studied. As shown in Fig. 1, the 1:15 scaled wind tunnel geometry model used was taken as the ***baseline*** (without any attachments). The design of the guide devices is shown in Fig. 2(a), comprising some long, curved, wedge-shaped blocks. In total, 17 wedge-shaped guide blocks were installed on the inner walls of the nozzle, which were evenly distributed, and the model has been defined as a ***wedge***, as shown in Fig. 2(b).

The ***baseline*** and ***wedge*** used the same setups, as follows. The numerical model was applied to the contraction part, the nozzle, the breathers, the plenum, the collector, the diffuser and the extend, as shown in Fig. 1. Two pressure reference points were set at the breathers and the reference pressure was set to standard atmospheric pressure. The 12 mm trimmed cell grid was used, and the boundary layer was a 10-layer grid with the first layer of 1 mm thickness and a growth rate of 1.1. The mesh sizes of the refinement areas were 3 mm and 6 mm, respectively, and their distribution is shown in Fig. 3. It

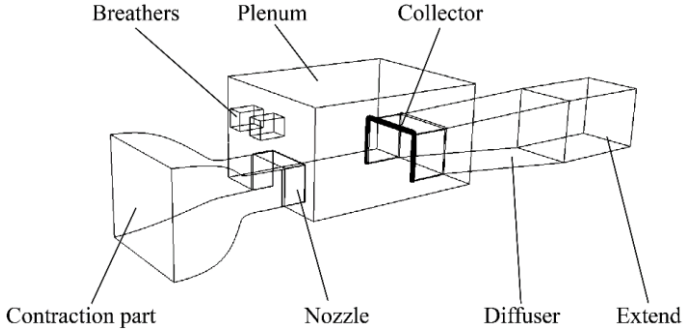

Fig. 1. Wind tunnel geometry of *baseline.*

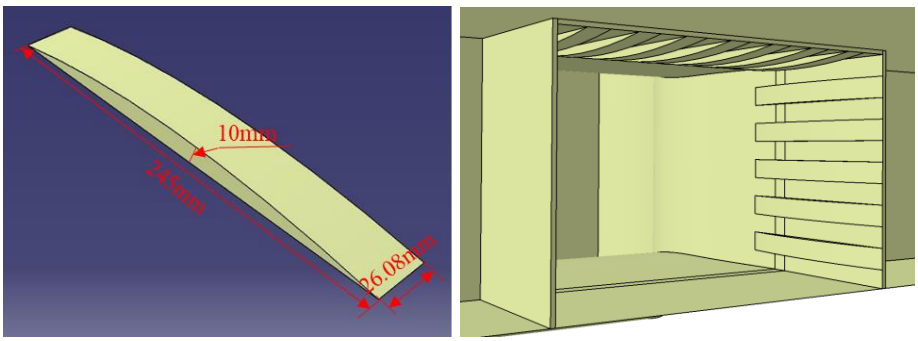

(a) (b)

Fig. 2. Guide devices and *wedge* nozzle.

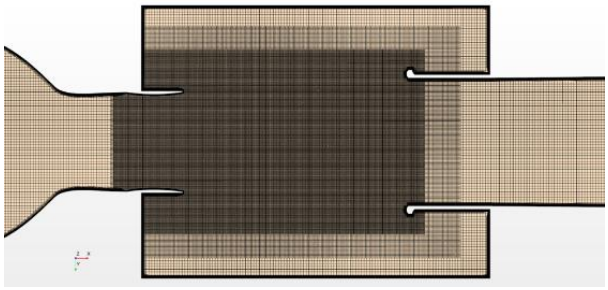

Fig. 3. Mesh distribution overview.

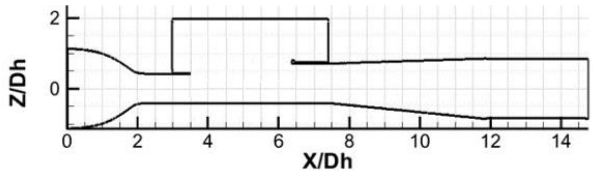

Fig. 4. Mid-section of the wind tunnel in D_h.

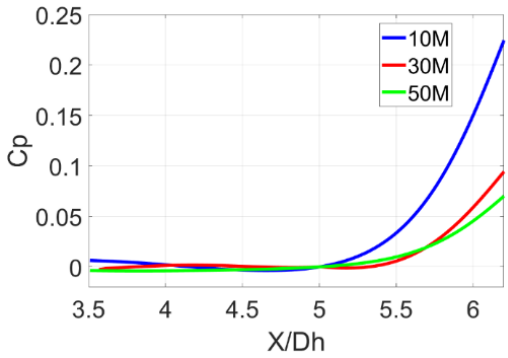

Fig. 5. The pressure gradient of the 3 meshes in the test section.

was guaranteed that $y^+ < 1$, x^+ and $z^+ < 50$ .The number of grid cells in the ***baseline*** was 33246070, and that in the ***wedge*** was 36138190. The measured inlet turbulence intensity of the 1:15 model wind tunnel was 0.01. According to the previous study of Zheng & Yang (2008), the flow speed with the most obvious low-frequency buffeting phenomenon was selected: the inflow velocity was 25 m/s at the nozzle, $Re = 5.7 \times 10^5$. The equivalent hydraulic diameter of the nozzle was $D_h = 0.342m$.

Through the previous works of Rashidi et al. (2019) and Zheng (2009) on the low-frequency buffeting phenomenon of a 3/4 open-jet recirculation wind tunnel, we find that the phenomenon of low-frequency buffeting is the most obvious when the wind tunnel has a collector opening angle of 0°. As such, the research was carried out with the angle of the collector set at 0°.

The steady simulation adopted a Realizable K-Epsilon viscosity turbulence model and two-layer all y^+ wall treatment. The large eddy simulation (LES) was used for the unsteady simulation. The LES adopted the WALE Subgrid Scale model, all y^+ treatment and the implicit unsteady model. This paper's numerical simulation was performed with the commercial CFD software STAR-CCM+. The simulation model used a separate compressible solver. The boundary-centered difference scheme and the second-order upwind discrete scheme were respectively used for the diffusion terms and the convection terms. Data sampling started after the unsteady simulation became stable at 0.5 s; the total sampling time was 2.5 s and the time step was $5 \times 10^{-5}s$.

2.2 Mesh Convergence Study

In order to ensure that the mesh was sufficiently fine and the simulation results were independent of the mesh, a study with different mesh resolutions was carried out, with mesh cells of 10 million, 30 million, and 50 million. The number of cells was mainly determined by adjusting the overall base size of the grid. All simulations used the same settings as described in Section 2.2, based on the ***baseline***. The axial static pressure gradient in the test section of the wind tunnel is an important indicator of the uniformity of the flow field. Therefore, on the axial symmetry plane of the test section of the simulation, 200 measuring points were uniformly distributed from the nozzle to the collector at a height of 50 mm ($Z/D_h = -0.268$) from the ground. Fig. 4 shows the dimensionless geometry of the wind tunnel's mid-section.

Fig. 5 shows the pressure gradient given by Eq. (1) for three mesh resolutions. There was not much difference between the curves of 30 M and 50 M. Since the test model is usually placed at X/Dh = 4~5.5, the static pressure gradient within this interval is expected to remain consistent. The region with X/Dh > 6 is part of the wake region near the collector, and the variation of the static pressure gradient is within an acceptable range when the mesh number is more than 30 million. Considering both the accuracy and efficiency of the simulation, the mesh count was set at approximately 30 million. This validates

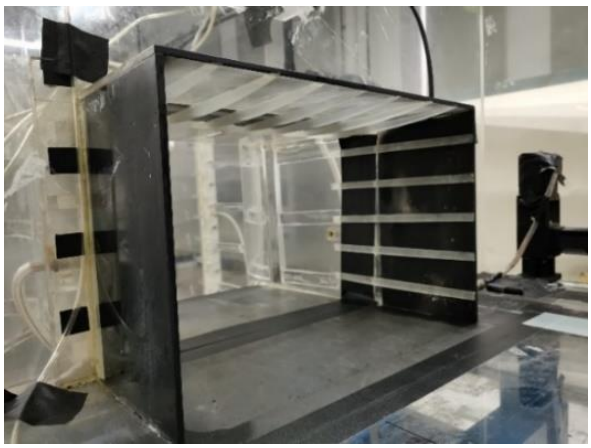

Fig. 6. Guide devices installed on the inner wall of the nozzle.

the mesh convergence and independence of the simulations using a 30 million-cell mesh.

$$C_p = \frac{P_s - P_{0s}}{P_{0d}} \tag{1}$$

Here, P_s—static pressure, P_{0s}—static pressure of the reference point, P_{0d}—dynamic pressure of the reference point. The intersection points of three planes $Y/D_h = 0$, $Z/D_h = -0.268$ and $X/D_h = 5$ were selected as the reference points.

2.3 Experimental Setup

The experiment was carried out in the 1:15 model wind tunnel at the SAWTC. The size of the plenum was 1517 mm × 1185 mm × 818 mm (length × width × height). The width of the nozzle was 433 mm and the height was 283 mm. The distance between the nozzle and the collector was 1000 mm. The flow direction turbulence intensity was 0.01. The angle of the collector was 0°. The room temperature during the test was 20.4 °C, and the atmospheric pressure was 100921 Pa. In total, 17 guide devices were constructed from plexiglass via wire-cutting, and these were set on the inner wall of the nozzle, which is shown in Fig. 6.

Before the test, the wind speed required by each working condition was measured and calibrated with a pitot tube, and the calibration point was selected as the center of the nozzle outlet.

2.3.1 Isothermal Hot Wire Anemometer Speed Test

A one-dimensional hot wire probe (Model 55P01) provided by Dantec Company was used in the test, the overheat ratio was 1.4, the sampling frequency was 1000 Hz, and the sampling time was 8 s. After calibration with the Dantec Streamline Pro Automatic Calibrator, the relative error of the velocity measurement was found to be ±1.5%. The temperature variation in the test section was less than 0.5 ° C during the test. The layout of the measuring points is shown in Fig. 7. The points of the test section started from a position 20 mm away from center of the nozzle, and each was arranged 50 mm along the flow direction, for a total of 14 points. The points were numbered sequentially from point 1 to point 14 along the flow direction, and a one-dimensional probe was used to capture the downstream velocity.

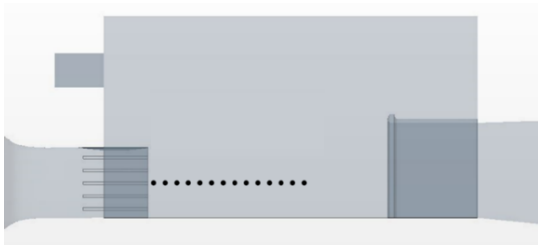

Fig. 7. Layout of measuring points for hot wire test.

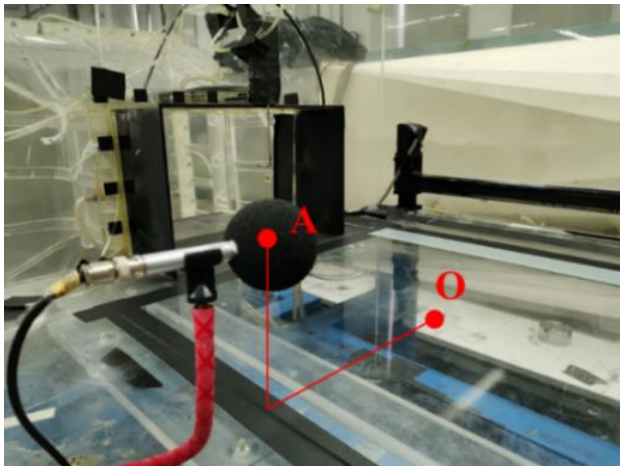

Fig. 8. Layout of the test point for sound pressure level test.

2.3.2 Sound Pressure Level Test

The equipment used for acoustic measurements included GRAS microphones (including preamplifiers), a B&K standard acoustic calibrator and Artemis, and a multi-channel acoustic test analysis system from HEAD Acoustics. The sensitivity of the free-field microphone was 50 mV/Pa, and the uncertainty of the microphone test was ±0.08 dB after calibration using a standard acoustic calibrator. As shown in Fig. 8, in order to measure the noise characteristics of the far-field outside the jet shear layer, the test point was set at point A, 500 mm away from the midpoint O in the x direction of the test section, and 100 mm away from the floor of the plenum. Before the test, the microphone was calibrated with a standard acoustic calibrator, and the inflow velocity was calibrated via a pitot tube. The measurement was started after the flow was stable. The sampling frequency of the microphone channel was 48 kHz, and the sampling time was 10 s.

3. Numerical Results of Baseline and Wedge

3.1 Baseline

There are different varieties of flow structures in the jet shear layer that interact with each other in a complex manner. It is difficult to analyze the typical flow characteristics using the transient velocity field alone. Proper Orthogonal Decomposition (POD) is mainly used to extract the main modes during multi-dimensional data set processing (Cazemier et al., 1998).

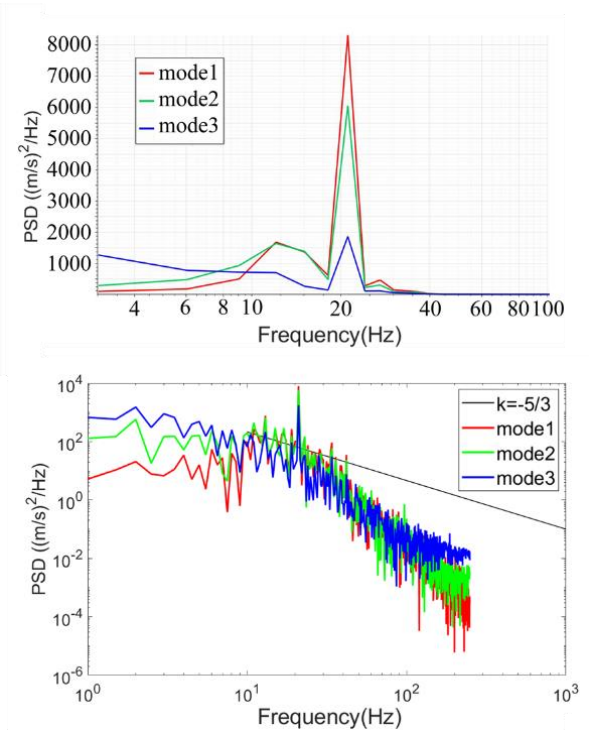

Fig. 9. The first 3 velocity modes spectrum of *baseline*.

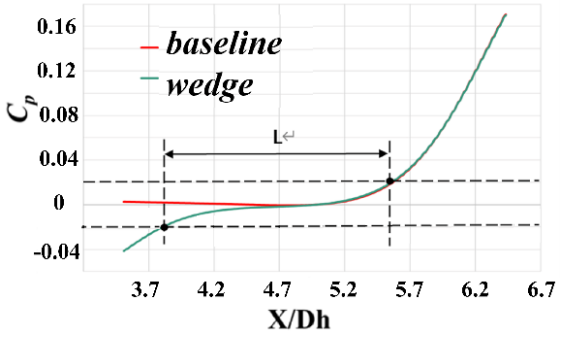

Fig. 10. The axial static pressure gradient C_p of *baseline* and *wedge*.

The 2-d POD analysis of the U (x-axis) and W (z-axis) velocity components in the sampling area of the cross-section was carried out. The dimensionless size of the sampling area was length—$3.571 < X/D_h < 6.255$ and height— $-0.413 < Z/D_h < 1.100$ (including the flow field from the nozzle to the collection port). The POD analysis selected 1000 instantaneous velocity snapshots with a sampling frequency of 1000 Hz, and the total sampling time was 1 s.

The first three modes of the flow field were extracted by means of POD, then Fast Fourier transform (FFT) spectrum analysis was applied to the first three modes' time coefficients, and the frequency spectrum is shown in Fig. 9. The first three modes of ***baseline*** all had the same peak frequency of 21 Hz. Obvious low-frequency buffeting occurred. As the natural vortex separated from the nozzle, the large vortexes traveled downstream and hit the collector, forming Edgetone-Type Feedback. The frequency of the vortex separation was determined by the Edgetone-Type Feedback frequency, and this formed the Rossiter mode (Rossiter, 1964; Bartel & McAvoy 1981). The second mode frequency was 23.99 Hz, which is close to the Helmholtz resonance frequency (Von Helmholtz, 1912) of 21.3 Hz, resulting in a resonance phenomenon and vortex separation frequency being limited to 21 Hz. The bottom of Fig. 9 shows the PSD of the first three modes of velocity on a log–log scale. The velocity modes show a broad decay region, consistent with the inertial subrange, with a slope less than the typical—5/3—determined by Kolmogorov theory, which suggests that the current grid size setting provided a good resolution. (The spectral range is truncated at 500 Hz because the sampling frequency was 1000 Hz.)

3.2 Wedge

3.2.1 The influence of Guide Devices on Characteristics of the Flow Field

The 200 pressure gradient measuring points were distributed in the same manner as in Section 2.2. The curve of the axial static pressure gradient in the test section is shown in Fig. 10.

It can be seen from Fig. 10 that due to the existence of guide devices, the local airflow close to the nozzle was accelerated, which caused the dynamic pressure of the nozzle to increase and the static pressure to decrease. The axial static pressure gradient became negative, and the uniformity of the flow field became worse. However, far away from the nozzle, the axial static pressure gradient changed little, and the two curves almost coincided.

Due to the presence of the guide devices, the natural vortex separation at the nozzle was undone in advance while moving downstream. This was due to the acceleration of the flow near the guide devices, resulting in a static pressure difference between the guide devices. The airflow was deflected. These factors led to the formation of longitudinal vortexes, which interfered with the natural vortex separation near the nozzle and destroyed their structures. Fig. 11 shows a three-dimensional vorticity nephogram of the cross-section of ***wedge*** at $X/D_h = 3.6$. It can be seen that vortex structures perpendicular to the axis of the natural vortexes were produced at the nozzle.

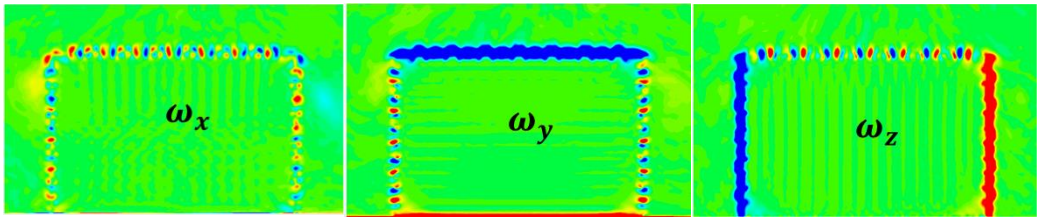

Fig. 11. Three-directional vorticity nephogram of the cross-section of the *wedge* at $X/D_h = 3.6$.

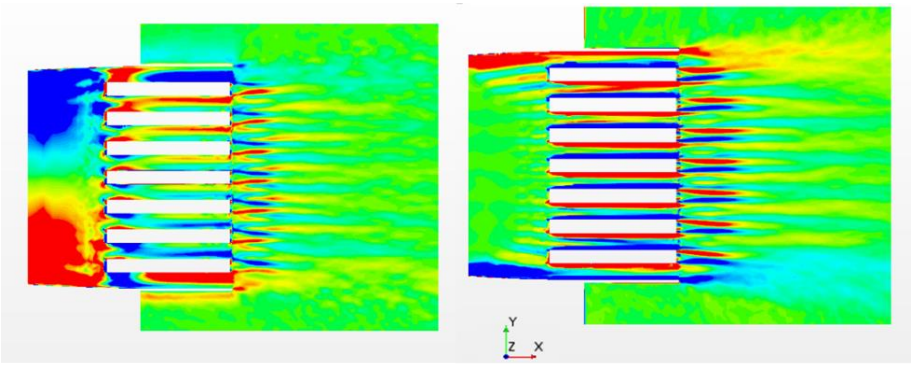

Fig. 12. X- and z-directional vorticity nephogram of the *wedge* on the z section at $Z/D_h = 4$.

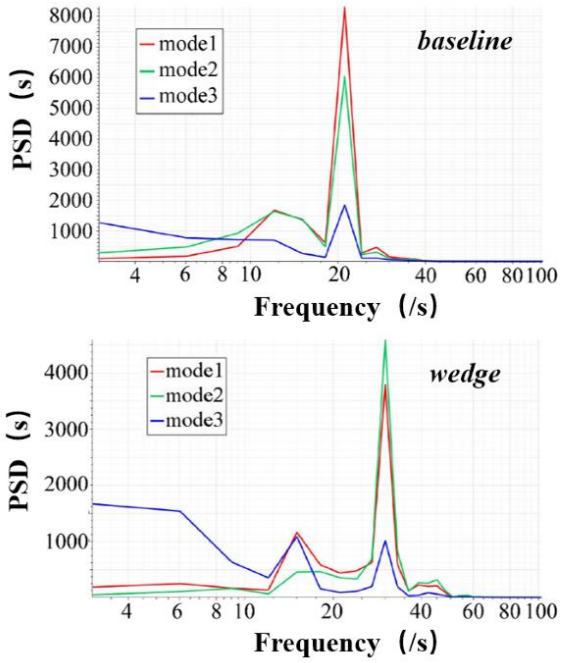

Fig. 13. The first 3 velocity modes' spectrum.

The x and z components of the vorticity nephograms on the z section at $Z/D_h = 4$ are shown in Fig. 12. Looking at Fig. 11 and Fig. 12, it can be seen that strong x- and z-directional vortexes were generated between the guide devices, which would interact with the natural vortex separation in the y-direction at the nozzle. Thus, the Edgetone-Type Feedback was altered as the large-scale vortex structures were destroyed by the vortexes generated by the guide devices.

3.2.2 The influence of *wedge* on the Velocity in the Jet Shear Layer

The 2-d POD analysis of the U (x-axis) and W (z-axis) velocity components in the sampling area of the cross-section was carried out in the same manner as above.

FFT spectrum analysis was applied to the first three modes' time coefficients, and the frequency spectrum is shown in Fig. 13. It can be seen that the first, second and third modes of ***wedge*** had the same main peak frequency of 30 Hz, and the second peak frequency of 15 Hz. These frequencies correspond to the first-order and second-order

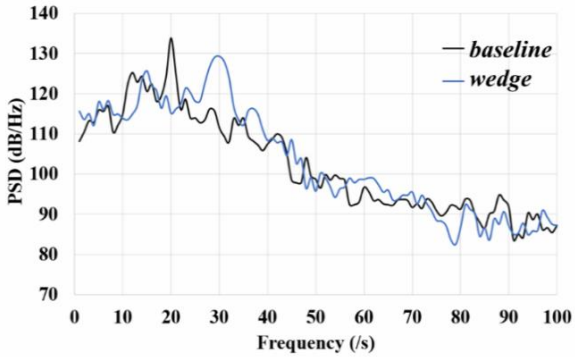

Fig. 14. The spectrum (dB/Hz) of *baseline* and *wedge/*.

Edgetone-Type Feedback frequencies of the model wind tunnel, which are $f_{f1} = 15.432Hz$ and $f_{f2} = 30.906Hz$.

The first three modes of ***baseline*** all had the same peak frequency of 21 Hz, as shown in Fig. 13, and the peak of the Power Spectrum Density (PSD) was also very high. The previous research results show that the low-frequency buffeting of the model wind tunnel under low-speed conditions was about 21 Hz (Zheng, 2009). The installation of the guide devices reduced the excitation of the natural frequency of the modes, and deviated the peak frequency from the sensitive frequency (21 Hz) of the low-frequency buffeting. The original large-scale vortex structures at the nozzle were disrupted due to the longitudinal vortexes produced by the guide devices, and were broken into smaller vortexes. This partly weakened the pressure wave and large vortex feedback; thus, the peak frequency and peak value were altered by the ***wedge***.

However, due to the interference of the guide devices, the original vortex structures of the nozzle were destroyed, and the flow field from the nozzle to the collector formed a mode similar to the second-order Edgetone-Type Feedback, which attained a frequency of around 30 Hz. Though the ***wedge*** partly reduced the low-frequency buffeting phenomenon, a main peak still occurred. Fig. 14 shows the frequency spectrum (in dB) of the ***baseline*** and the ***wedge***. A peak can be seen at around 20 Hz in the ***baseline*** due to the low-frequency buffeting, which was eliminated in the ***wedge***. However, there was a large increase in dB at around 30 Hz in the ***wedge***. This case thus failed to meet the design requirements of our target.

4. EGM OPTIMIZATION

4.1 Optimization of the Guide Devices with EGM

The guide devices designed by experience generally may not meet the optimal targets. In order to achieve a better design, a more effective optimization algorithm was applied. Based on the EGM, the optimization of the guide devices can be carried out (Li et al., 2022). The optimization aimed to reduce the low-frequency buffeting phenomenon while ensuring good flow field uniformity.

The main optimization target was to improve the uniformity of the flow field in the test section by optimizing the shape of the guide devices, which raised an optimization problem in high-dimensional parameter space. To solve the above optimization problem with an acceptable computational cost, the choice of the optimization algorithm was vital. For example, the genetic algorithm, a classical optimization algorithm, improves the success rate of convergence to the global optimal solution via four genetic operations: elitism, reproduction, crossover, and mutation. However, its convergence speed and actual convergence are not guaranteed. This problem is more prominent in optimization with a larger number of individual evaluations or with higher dimensionality of the optimization parameters. The individual tests in this section were performed via computationally expensive CFD, and the genetic algorithm was not applicable as it is prone to wasting computational resources.

The Downhill Simplex Method, the representative and most robust algorithm for gradient searching, uses the gradient information of the surrounding points to descend to a local optimum with high efficiency and good convergence, but the algorithm easily falls into a local optimum (Press et al. 2007). Latin sampling explores the entire domain independently of the cost, and is clearly more likely to approach the global minimum. LHS explores the entire domain independently of the cost and is clearly more likely to approach the global optimum (McKay et al., 2000).

Therefore, Li et al. (2022) designed and proposed a novel algorithm to achieve an efficient optimization search, represented by the EGM used in this section. The EGM was developed from the idea of the genetic algorithm. When dealing with high-dimensional parameter space, it explores a local area using the Downhill Simplex Method; meanwhile, it explores uniformly throughout the parameter space by means of LHS. The steps of the method, in brief, are as follows:

a) **Initialization.** Obtaining *M* initial individuals for the Downhill Simplex Method;

b) **Downhill simplex.** Performing one simplex iteration based on the best *M*+1 parameters discovered so far;

c) **LHS.** Computing the cost of a new LHS parameter. Taking a parameter that is farthest from all current parameters;

d) **Loop.** Back to **a)** for the next loop until a convergence result is found.

For more details on the EGM, refer to Li et al. (2022)

Although in the preliminary study on the ***wedge*** it was found that the guide devices can effectively reduce low-frequency buffeting, the change in the axial static pressure gradient in the test section increased, and the uniformity of the flow field became worse. Therefore, the optimization of the guide devices was pursued.

The length L_g, width W_g and height H_g of the guide devices were selected as the three parameters for shape optimization. Considering the length of the model wind tunnel nozzle, the range of L_g was 100-280 mm, and considering the possible interference between the guide devices at the corner of the nozzle, the range of W_g was 10-40 mm, while that of H_g was 10-20mm.

It was necessary to ensure the uniformity of the flow field in the test section, which roughly corresponded to the range of $3.509 < X/D_h < 5.556$ in the 1:15 scale wind tunnel. The optimization approach aimed to improve the variation of the axial static pressure gradient within this range. As shown in Fig. 10, the axial static pressure gradients of the test section ($3.509 < X/D_h < 5.556$) of the ***baseline*** were all less than 0.02. Considering that the static pressure gradient around the guide devices was negative after its installation, ±0.02 was taken as the threshold value for the axial static pressure gradient. The longer the length L_c covered by the axial static pressure gradient curve within the threshold, and the smoother the curve is, the better the uniformity of the flow field. The optimization sought to make the cost function converge to a smaller value, so $1/L_c$ was set as the cost function. During optimization, the cost function $1/L_c$ was calculated by RANS simulations during each loop. When the optimization converged, the value of the cost function $1/L_c$ was the lowest, the axial static pressure gradient curve of the optimal case was the smoothest, and its flow field uniformity was also the best.

According to EGM optimization, four initial cases were given, their axial static pressure gradient curves were obtained by steady numerical simulation, and their respective cost functions were also calculated. The information is shown in Table 1.

The convergence error precision was set to 0.0005. After 12 rounds of optimization, the algorithm converged to the optimal solution, which was defined as ***wedge-optimized***. The size and the cost function of the guide devices are shown in Table 2. The axial static pressure gradient of the optimal case is shown as the green curve in Fig. 15 and the coverage of the curve within the threshold was $3.509 < X/D_h < 5.585$.

Table 1 Initial cases of EGM optimization

Case	L_g (mm)	W_g (mm)	H_g (mm)	$1/L_c$
1	190	25	15	0.560656
2	100	10	20	0.495652
3	100	40	10	0.605310
4	280	10	10	0.488571

Table 2 The optimal case of the guide devices

L_g(mm)	W_g(mm)	H_g(mm)	$1/L_c$
273.67	10.82	10.35	0.481690

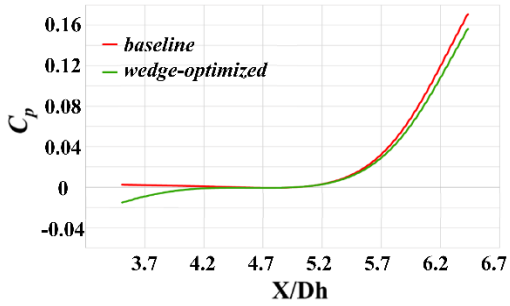

Fig. 15. Comparison of the optimal case axial static pressure gradient with the *baseline.*

4.2 Simulation Results of the *Wedge-Optimized*

4.2.1 Steady flow Field Characteristics of the Optimal Case

The analysis of ***wedge-optimized*** and ***baseline*** was based on 1500 flow field snapshots with a sampling frequency of 1000 Hz. The time-averaged downstream velocity nephogram and turbulence intensity nephogram are shown in Fig. 16, Fig. 17 and Fig. 18. Three sections were investigated: Y_0 : the mid-section of $Y/D_h = 0$, Z_0 : the cross-section of $Z/D_h = 0$, $Y_{+0.18}$: the section located 0.18 meters from Y_0 (near the wall of the nozzle).

Fig. 16 shows that the core flow area (≥0.95) of the ***wedge-optimized*** basically maintained its original size, which was 6.2 times that of the hydraulic diameter in the Y_0 section. In all three sampling sections, the downstream velocity nephogram of the ***wedge-optimized*** was almost the same as that of the ***baseline***. The ***wedge-optimized*** generally preserved its original average velocity characteristics.

The downstream turbulence intensity values of the ***wedge-optimized*** and ***baseline*** are shown in Fig. 17. In the Y_0 and $Y_{+0.18}$ sections, ***wedge-optimized*** showed significantly reduced downstream turbulence intensity compared to ***baseline*** in the jet shear layer ($Z/D_h = 0.4$), with a change from an initial value of 0.22 to approximately 0.16. Additionally, the area of the region where the turbulence intensity was greater than 0.2 also decreased in the jet shear layer. In the Z_0 section, the turbulence intensity (red area) of the ***wedge-optimized*** on both sides of the nozzle decreased significantly, and in the middle of the test section it decreased significantly from 0.04~0.06 to 0.02~0.04.

The vertical turbulence intensity values of the ***wedge-optimized*** and ***baseline*** are shown in Fig. 18. Similarly, there was a reduction in the high vertical turbulence region (represented by the red area) in the jet shear layer and an increase in the low turbulence region (0~0.04) in the test section.

Overall, the ***wedge-optimized*** flow exhibited a smaller turbulence region and a decrease in turbulence intensity.

4.2.2 Q-Criterion Analysis

Fig. 19 illustrates the ***baseline*** and ***wedge-optimized*** nephograms of the instantaneous Q-criterion for the horizontal cross-section ($Z/D_h = 0.4$) as well as the mid-section ($Y/D_h = 0$), with $Q \in [-50000, 50000]\ /s\hat{}2$.

In the $Y/D_h = 0$ section, near the nozzle of the baseline, three distinct narrow vortex rings are discernible, concentrated in the y-axis direction. This implies that the natural shedding vortex of the baseline nozzle was nearly two-dimensional and broke down as it propagated through the middle of the test section. The wedge-optimized nozzle only exhibited a long two-dimensional vortex ring structure near the nozzle, which was dispersed into numerous small, randomly distributed vortices by the guide devices.

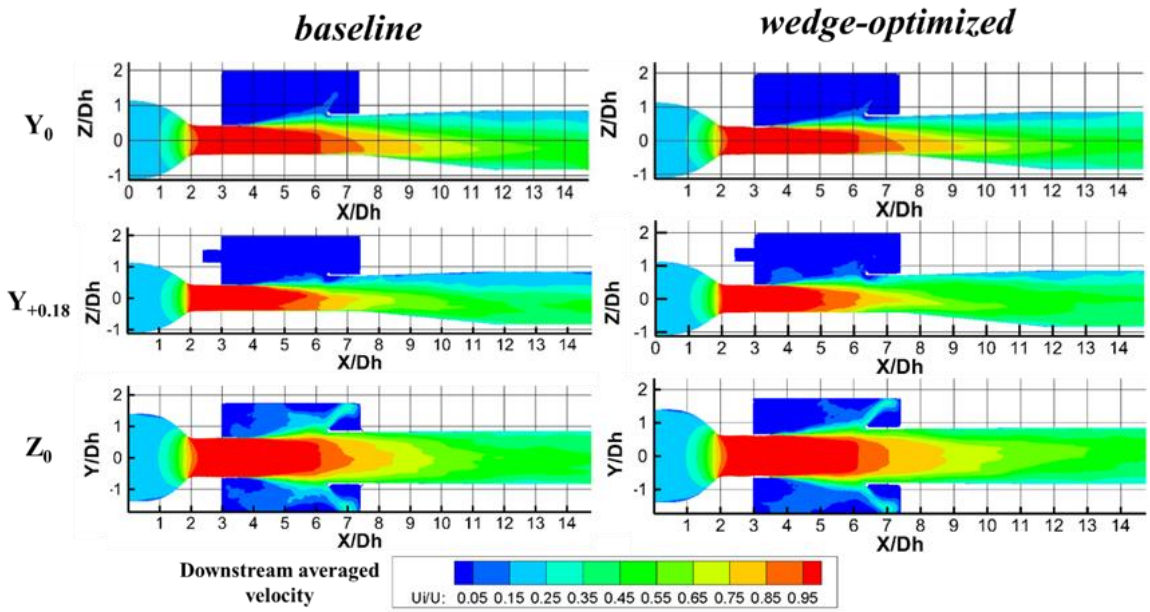

Fig. 16. Time-averaged downstream velocity of sampling sections.

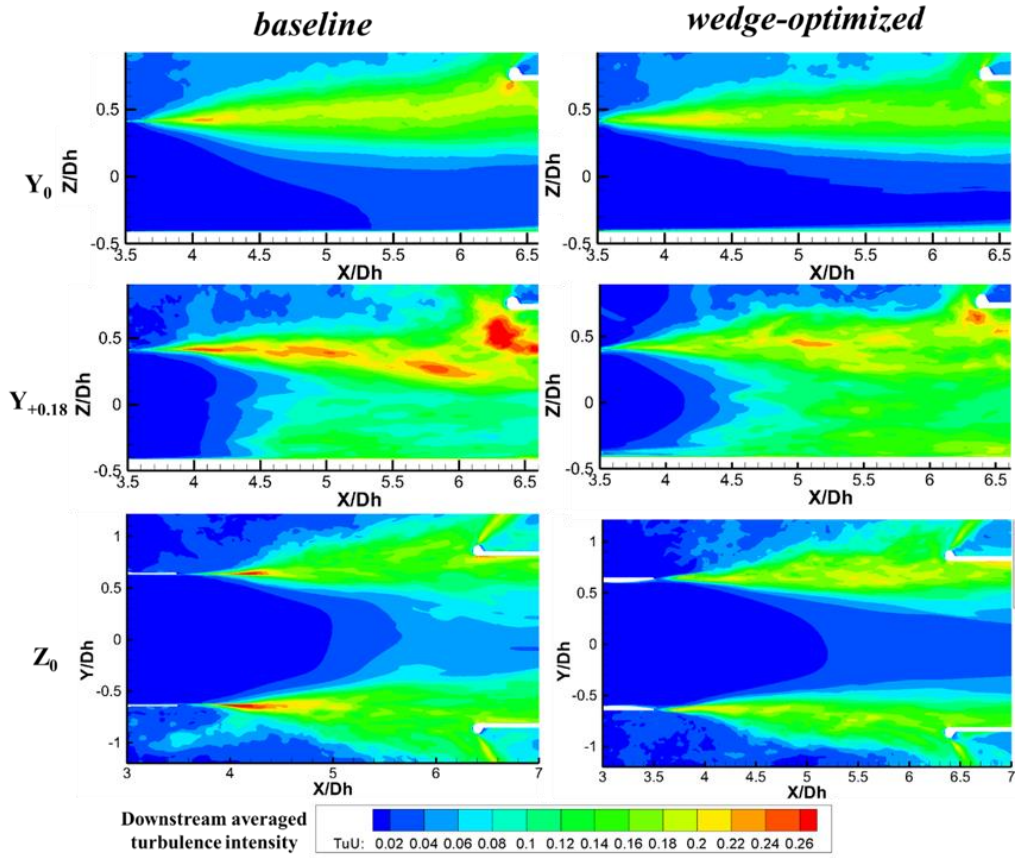

Fig. 17. Time-averaged downstream turbulence intensity of sampling sections.

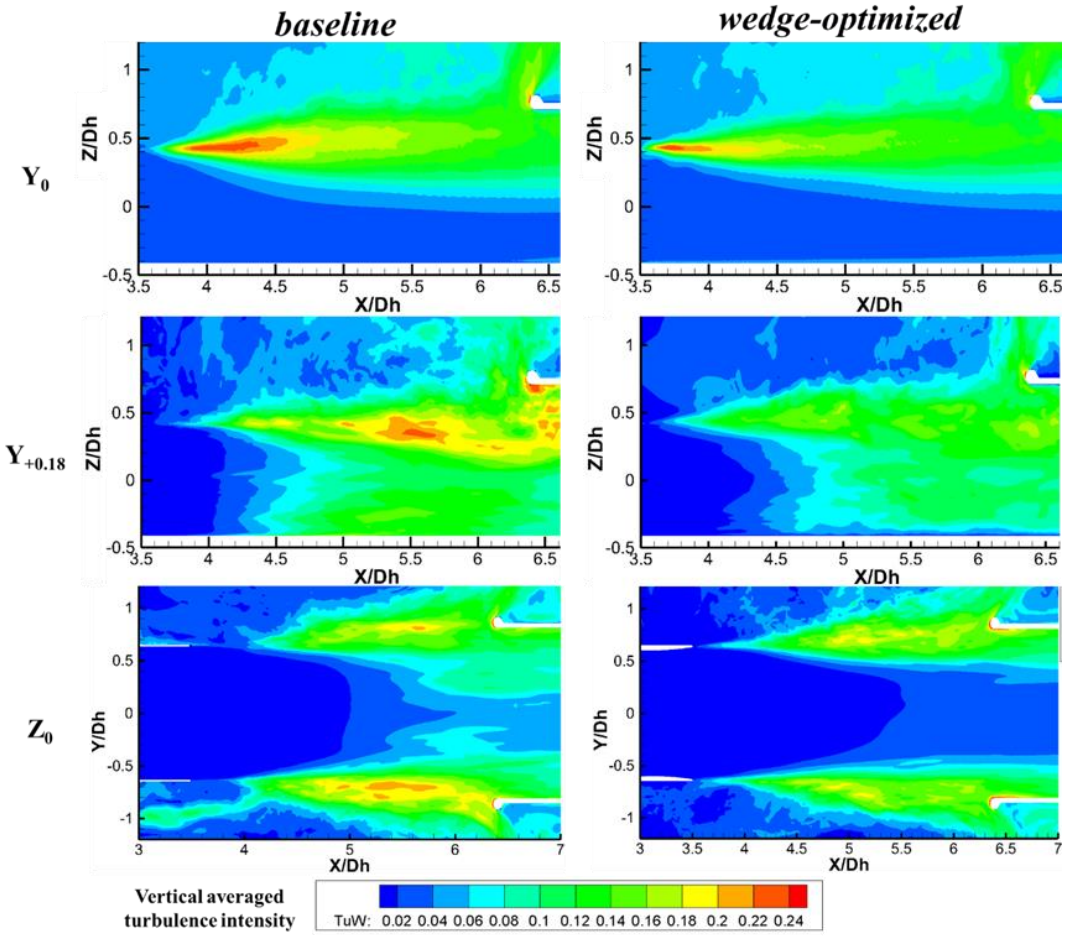

Fig. 18. Time-averaged vertical turbulence intensity of sampling sections.

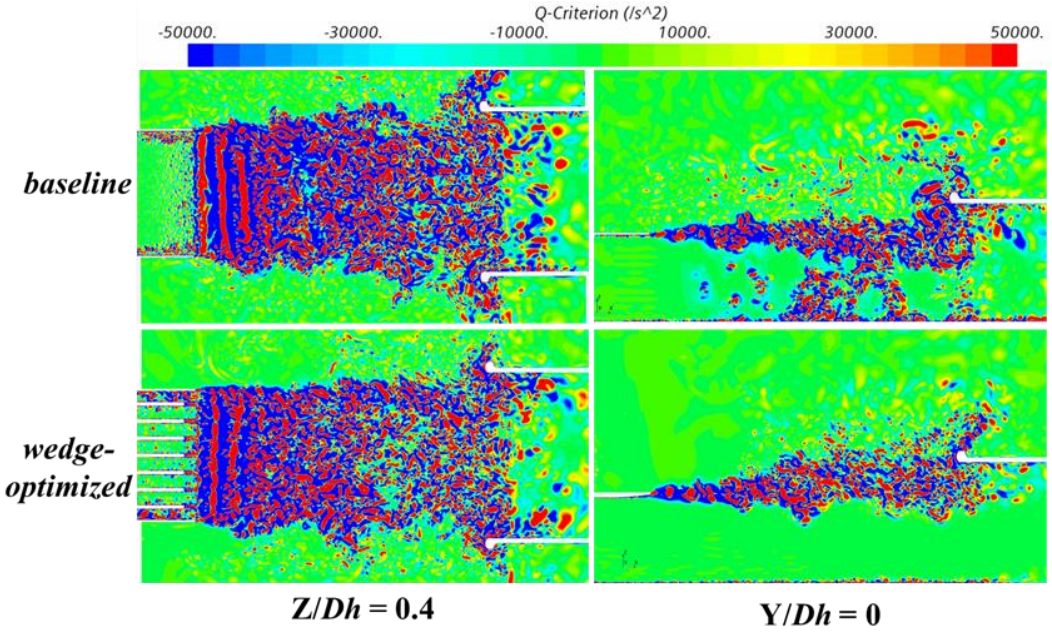

Fig. 19. Q-criterion nephograms of *baseline* and *wedge-optimized.*

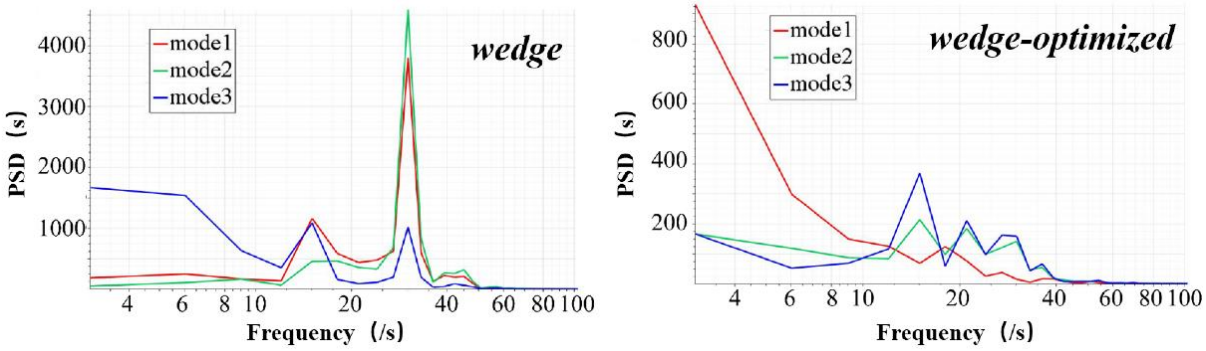

Fig. 20. Time coefficient spectrum of the first three velocity modes of *wedge-optimized* and *wedge.*

In the $Z/D_h = 0.4$ section, the large vortex structure of the baseline resulted in many broken vortex structures in the center of the test section, whereas the wedge-optimized effectively eliminated these vortices. The Q-criterion analysis of the jet shear layer reveals that the wedge-optimized effectively suppressed the resonant pulsations of velocity and pressure by disrupting the inducer of low-frequency fluctuation, which was the large-scale two-dimensional shedding vortices, thereby breaking the Edgetone-Type Feedback.

4.2.3 The Spectrum Analysis of the velocity in the jet shear layer

Similarly, POD analysis was performed on the two-dimensional velocity field (velocity components U and W) in the ***wedge-optimized*** sampling area. An FFT spectrum analysis was performed on the time coefficients of the first three modes, which is shown in Fig. 20. It can be seen that modes 2 and 3 of the ***wedge-optimized*** had peaks at 15 Hz and 21 Hz. The value of the PSD at the peak frequency was only about 1/12 of that of the ***wedge*** and 1/21 of the ***baseline***. The peak frequencies of each mode of the velocity field were relatively scattered, meaning that ***wedge-optimized*** was more effective in suppressing the low-frequency buffeting phenomenon.

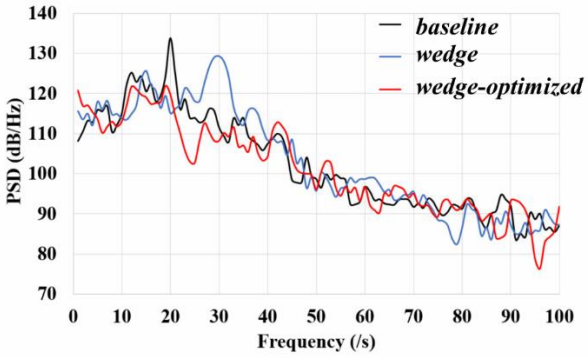

Fig. 21. The spectra (dB/Hz) of *baseline*, *wedge*, and *wedge-optimized.*

The spectra (in dB) of ***baseline***, ***wedge***, and ***wedge-optimized*** are shown in Fig. 21. The disappearance of peaks around 20 Hz and 30 Hz shows that ***wedge-optimized*** not only reduced the original low-frequency buffeting, but also eliminated the peak around 30 Hz caused by the deficiency in the ***wedge*** design. At other frequencies, ***wedge-optimized*** maintained a dB/Hz level similar to that of ***baseline***.

In conclusion, the optimal solution ***wedge-optimized*** obtained by the EGM can efficiently suppress the

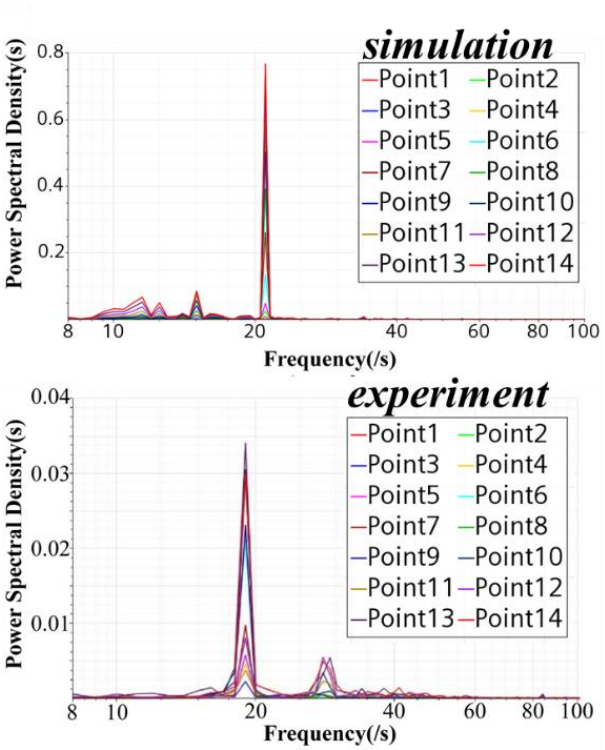

Fig. 22. Simulation and experiment FFT results of *baseline.*

occurrence of low-frequency buffeting, and also ensure the uniformity of the flow field in the test section.

5. EXPERIMENT RESULTS

5.1 Hot-wired Test Results

The hot wire test was used to measure the working conditions before and after the installation of the devices. The inflow speed was set to 25 m/s, the same as the numerical simulation, and the Reynolds number $Re = 5.7 \times 10^5$. FFT analysis was performed on the instantaneous speed of each measuring point.

The spectrum validation of ***baseline*** is shown in Fig. 22. The simulation and experiment both found the main frequency of low-frequency fluctuation around 20 Hz. In addition, a small peak of about 30 Hz was found in the experiment, which may be due to the fact that a partial model of the wind tunnel was used, and some more complex mechanisms were overlooked. This shows that the simulation settings were able to capture the main frequencies of low-frequency fluctuation. The discrepancy between the experimental and simulated peak values indicates that the velocity pulsation phenomenon is significantly weaker in reality. In a return-type wind tunnel, the airflow passes through the fan and exits the nozzle after passing through various devices. Even with the use of damping screens and honeycomb devices to stabilize the flow, the velocity at the nozzle and the intensity of turbulence near the wall still exhibit a certain degree of spatial and temporal inhomogeneity in their distribution. However, the boundary layer setting in the simulation is simplified to make it homogeneous, resulting in more concentrated vortex shedding at the nozzle and a more obvious low-frequency fluctuation phenomenon,

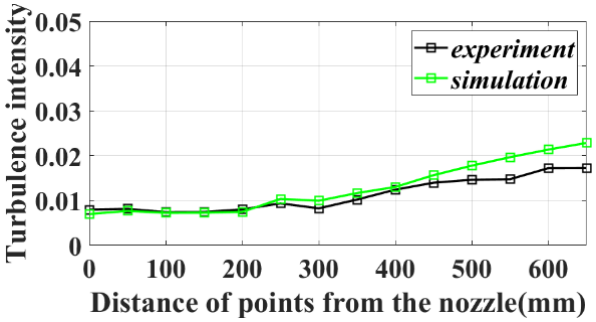

Fig. 23. Turbulence intensity validation of *baseline.*

leading to a larger pulsation amplitude in the simulation. This can be further investigated in future studies focusing on the impact of non-uniform incoming flow on low-frequency chattering.

The turbulence intensity validation of the ***baseline*** measuring points is shown in Fig. 23 for point 1 to point 14 (0 mm to 650 mm). In the range of distances < 450 mm ($X/D_h < 4.8$), the simulated and experimental turbulence intensities matched well. However, for distances > 450 mm ($X/D_h > 4.8$), the experimental turbulence intensities were lower than the simulated values, with a difference of approximately 0.005 observed at point 14. The turbulence intensity in the latter half of the test section is lower in the experiment compared to the simulation results. This discrepancy is consistent with the previous spectral analysis, wherein the experiment was less affected by low-frequency fluctuation compared to the simulation, as indicated by the smaller peak observed in Fig. 22. As seen in Fig. 19, many vortices were generated in the test section due to the strong low-frequency fluctuation in the simulation. These vortices caused the turbulence intensity in the latter half of the test section to be significantly elevated.

The spectrum of each measuring point of the ***baseline*** and ***wedge-optimized*** is shown in Fig. 24. The main peak frequency near 20 Hz and the secondary peak near 30 Hz are clear at each measurement point of the ***baseline***. Through the theoretical analysis of low-frequency buffeting, we identified obvious low-frequency buffeting in the model wind tunnel. After the implementation of the guide devices, the main peak frequency of each measurement point was changed from 20 Hz, the sensitive frequency of low-frequency buffeting, to about 30 Hz, and the power spectral density at 20 Hz dropped significantly. These changes suppressed the low-frequency fluctuation.

The turbulence intensity of the ***baseline*** and ***wedge-optimized*** measuring points is shown in Fig. 25. The turbulence intensity at the measurement points in the test section of the wedge-optimized was generally reduced compared to that of the b***aseline***. In the middle of the test section, where the test model was positioned (400~600 mm), the reduction in turbulence intensity is more noticeable compared to other parts of the test section. The average downstream velocity values of both are shown in Fig. 26, with U_0 being the inlet reference velocity of 25 m/s. A slightly higher average velocity can be seen at the nozzle (0-100 mm) in the ***baseline***. The velocity profile of the ***wedge-optimized*** is smoother compared to that of the

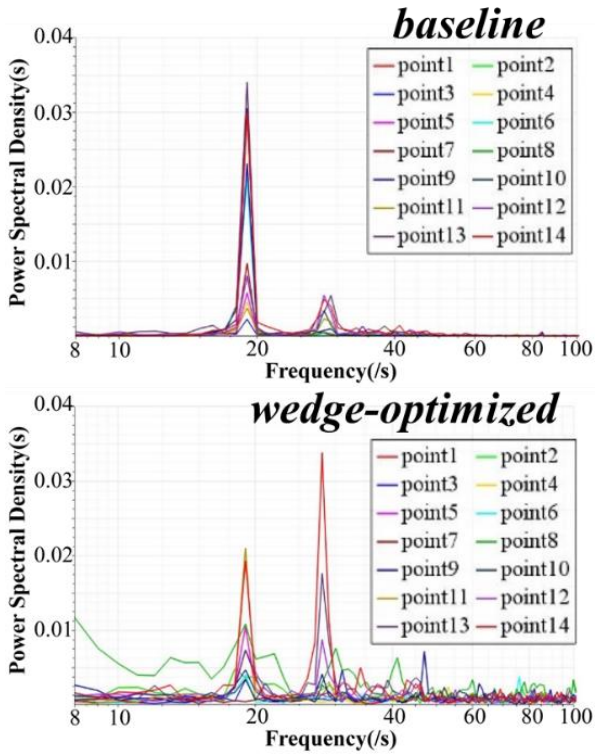

Fig. 24. Velocity FFT analysis of test section measuring points.

baseline, and the turbulence intensity in the test section is also lower, indicating that the presence of flow-guiding devices resulted in a more uniform flow field in the test section.

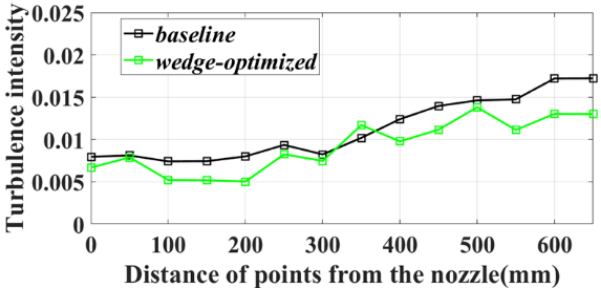

Fig. 25. Turbulence intensity values of *baseline* and *wedge-optimized* measuring points.

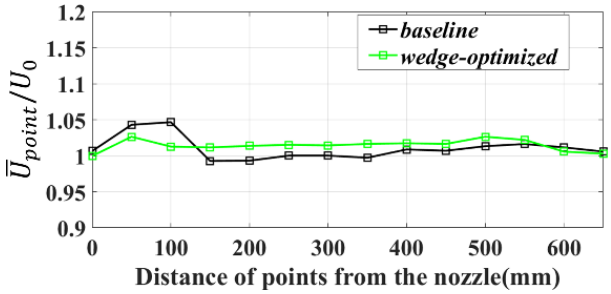

Fig. 26 Average downstream velocity of *baseline* and *wedge-optimized* mesuring points.

5.2 Sound Pressure Level Test Results

An FFT spectrum analysis was performed on the measurement results; the interception length of the spectrum analysis was 8192, the overlap rate was 50.0%, the Hanning window was selected as the window function, and the analysis of the 4-200 Hz frequency band was performed. The analysis results are shown in Fig. 27, where the ordinate is Sound Pressure Level (SPL). After the implementation of guide devices, the peak frequency was changed from the original 19.5 Hz to 29.3 Hz. At 19.5 Hz, the sound pressure level dropped 7.750 dB, from 99.281 dB to 91.531 dB, and at 29.3 Hz it dropped 1.086 dB. In most ranges of frequency, the spectral curve of ***wedge-optimized*** was below that of ***baseline***. The target of using guide devices is to reduce the deterioration of the sound and flow field caused by the low-frequency buffeting phenomenon in the wind tunnel at low frequencies (21Hz). Therefore, a drop in dB was observed around 20 Hz, which indicates that the guide devices largely met the requirements.

The Overall Sound Pressure Level (OASPL) was calculated for the whole frequency band using Eq. (2). The OASPL was reduced by 3 dB from 103.2 dB to 100.2 dB after installing the guide devices, which shows that the guide devices successfully suppressed the occurrence of low-frequency buffeting under the condition of 25 m/s.

$$OASPL = 10 \times \lg\left(\sum_{i=1}^{n} 10^{\frac{SPL_i}{10}}\right) \tag{2}$$

SPL_i is the SPL of point i.

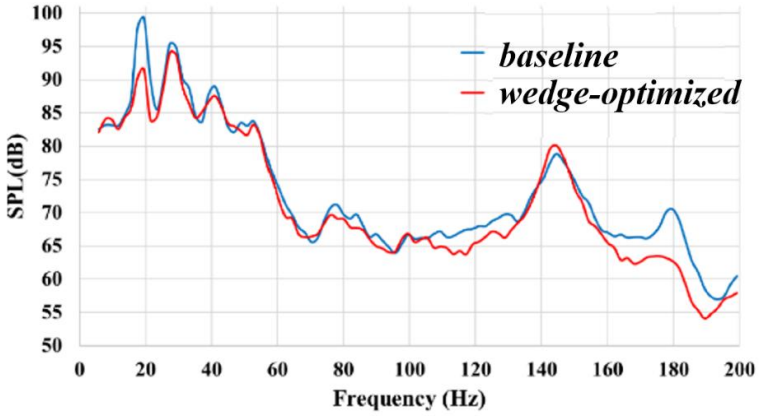

Fig. 27. Comparison of the Sound Pressure Level results.

6. CONCLUSIONS

(1) The original guide devices (***wedge***) partly suppressed the low-frequency fluctuation, but deteriorated the uniformity of the flow field. Due to the presence of guide devices on the inner wall of the nozzle, the inflow was affected and the boundary layer was separated in advance; the positions of nozzle vortex separation were also advanced accordingly. The guide devices partially deflected the airflow, but caused a static pressure difference between devices. These mechanisms produced vortexes on the side and top surfaces of the nozzle, which differed from the axis direction of the natural vortexes at the nozzle. The vortexes interacted with the natural vortexes and destroyed their structures, then interfered and paired with downstream vortexes in the jet shear layer, which led to the formation of different feedback loop excitations in the jet shear layer (30 Hz). The excitation frequency differed from the sensitive frequency whereat low-frequency buffeting occurred, thereby reducing the low-frequency buffeting phenomenon.

(2) The optimal case (***wedge-optimized***) obtained by the EGM for the guide devices was shown to effectively suppress the occurrence of low-frequency fluctuation, and also ensured the uniformity of the flow field in the test section. The steady and unsteady characteristics of the jet shear layer and the flow field in the test section were also significantly improved. Through the isothermal hot wire test and sound pressure level test, it was verified that the optimal case had a good inhibitory effect on the low-frequency buffeting phenomenon.

(3) According to the results, the design and EGM optimization of the guide devices applied in the model wind tunnel were effective. Later, a similar design and optimization process can be used to design and optimize similar guide devices in a full-scale wind tunnel, and the technique can be applied here too.

ACKNOWLEDGEMENTS

This work was supported by the Shanghai Automotive Wind Tunnel Technical Service Platform (Grand No. 19DZ2290400). Prof. Yang, Prof. Jia, and many students provided help with the theory and experiments of this paper. They are sincerely thanked for their help.

CONFLICT OF INTEREST

The authors declare that they have no known competing financial interests or personal relationships that could have appeared to influence the work reported in this paper.

AUTHORS CONTRIBUTION

Yikun Wang: Writing original draft, Investigation, Formal analysis, Validation, Writing - Review & Editing. Lei Huang: Writing original draft, Investigation, Formal analysis, Data curation, Validation. Qing Jia: Supervision, Methodology, Project administration, Funding acquisition, Writing - Review & Editing. Zhigang Yang: Conceptualization, Supervision, Project administration, Resources.

REFERENCES

Amandolèse, X., & Vartanian, C. (2010). Reduction of 3/4 open jet low-frequency fluctuations in the S2A wind tunnel. Journal of wind engineering and industrial aerodynamics, 98(10-11), 568-574. https://doi.org/10.1016/j.jweia.2010.04.011

Bartel, H. W., & McAvoy, J. M. (1981). *Cavity oscillation in cruise missile carrier aircraft.* Lockheed-Georgia Co Marietta Structures Technology Div.

Blumrich, R., Widdecke, N., Wiedemann, J., Michelbach, A., Wittmeier, F., & Beland, O. (2015). New FKFS technology at the full-scale aeroacoustic wind tunnel of University of Stuttgart. *SAE International Journal of Passenger Cars-Mechanical Systems*, 8(2015-01-1557), 294-305. https://doi.org/10.4271/2015-01-1557

Cazemier, W., Verstappen, R. W. C. P., & Veldman, A. E. P. (1998). Proper orthogonal decomposition and low-dimensional models for driven cavity flows. *Physics of Fluids*, 10(7), 1685-1699. https://doi.org/10.1063/1.869686

Evert, F., & Miehling, H. (2004). Active suppression of buffeting at the Audi AAWT: Operational experiences and enhancements of the control scheme. *SAE Transactions*, 419-430. https://doi.org/10.4271/2004-01-0804

Jia, Q., Huang, L., Zhu, Y., Rashidi, M. M., Xu, J., & Yang, Z. (2021). Experimental research of active control optimization on a 3/4 open-jet wind tunnel's jet section. *Alexandria Engineering Journal*, 60(2), 2265-2278. https://doi.org/10.1016/j.aej.2020.12.022

Künstner, R., Potthoff, J., & Essers, U. (1995). The aero-acoustic wind tunnel of Stuttgart University. *SAE Transactions*, 1119-1135.

Li, Y., Cui, W., Jia, Q., Li, Q., Yang, Z., Morzyński, M., & Noack, B. R. (2022). Explorative gradient method for active drag reduction of the fluidic pinball and slanted Ahmed body. *Journal of Fluid Mechanics*, 932. https://doi.org/10.1017/jfm.2021.974

McKay, M. D., Beckman, R. J., & Conover, W. J. (2000). A comparison of three methods for selecting values of input variables in the analysis of output from a computer code. *Technometrics*, 42(1), 55-61. https://doi.org/10.2307/1268522

Nelder, J. A., & Mead, R. (1965). A simplex method for function minimization. *The computer Journal*, 7(4),

308-313. https://doi.org/10.1093/comjnl/7.4.308

Pott-Pollenske, M., Von Heesen, W., & Bergmann, A. (2012). *Acoustical preexamination work and characterization of the low noise wind tunnel DNW-NWB.* 18th AIAA/CEAS Aeroacoustics Conference (33rd AIAA Aeroacoustics Conference). https://doi.org/10.2514/6.2012-2175

Press, W. H., Teukolsky, S. A., Vetterling, W. T., & Flannery, B. P. (2007). *Numerical Recipes 3rd Edition: the Art of Scientific Computing*. Cambridge university press.

Rashidi, M. M., Jia, Q., Yang, Z., Bao, D., & Zhu, Y. (2019). On the low frequency pressure fluctuation in a 3/4 open jet automotive wind tunnel. *Journal of Applied Fluid Mechanics*, 12(5), 1359-1369. https://doi.org/10.29252/jafm.12.05.29530

Rossiter, J. E. (1964). Wind-tunnel experiments on the flow over rectangular cavities at subsonic and transonic speeds.

Stoll, D., & Wiedemann, J. (2018). Active Crosswind Generation and Its Effect on the Unsteady Aerodynamic Vehicle Properties Determined in an Open Jet Wind Tunnel. *SAE International Journal of Passenger Cars-Mechanical Systems*, 11(5), 429-447. https://doi.org/10.4271/2018-01-0722

Von Helmholtz, H. (1912). *On the Sensations of Tone as a Physiological Basis for the Theory of Music*. Longmans, Green.

Zheng, Z. (2009). *Study and control of buffeting phenomenon for automotive aero-acoustic wind tunnel*. [Master's Thesis, Tongji University]. Shanghai, China. [in Chinese].

Zheng, Z., & Yang, Z. (2008). *Experimental Investigations of Effects of Collector on Performances of Automotive Wind Tunnel* (No. 2008-01-1206). SAE Technical Paper.